Chemical Science

ROYAL SOCIETY OF CHEMISTRY

EDGE ARTICLE

View Article Online
View Journal | View Issue

Cite this: *Chem. Sci.*, 2025, **16**, 22666

All publication charges for this article have been paid for by the Royal Society of Chemistry

Ladder-type phenazine-linked covalent organic polymers with synergistic cation–π interactions for highly stable lithium metal batteries

Xiao-Meng Lu,† Haichao Wang,† Yiwen Sun, Yi Xu, Yang Wu, Weiwei Sun, Chao Yang, Yifan Zhang and Yong Wang *

Received 2nd September 2025
Accepted 19th October 2025

DOI: 10.1039/d5sc06777d

rsc.li/chemical-science

The construction of an efficient regulating film for lithium metal anodes, capable of addressing both dendritic growth and by-product reactions, is pivotal to the stability of lithium metal batteries. Herein, a ladder-type phenazine-linked covalent organic polymer (PZ-CHPT) with a fully extended two-dimensional aromatic π-conjugated system, enriched with nitrogen sites (C–C=N–C linkages, C=N units), is introduced as a lithium metal anode protective layer to control spatial ion flux and induce uniform charge distribution, aiming at enhancing the reliability of lithium metal batteries. Remarkably, the incorporation of rigid heterocyclic units into PZ-CHPT boosts interfacial stability through reinforced covalent linkage strength and reduces Li^+ diffusion energy consumption, while the concurrent cation–π interactions between Li^+ and electron-rich aromatic motifs dynamically polarize the π-electron distribution, ultimately establishing continuous ion-transfer pathways through electrostatic-guided hopping along the conjugated framework, as validated by multimodal characterization techniques. Leveraging these synergistic properties, the PZ-CHPT-based full cells retain an exceptional 86.1% capacity after 1800 cycles at 3C, showing a minimal cycle-to-cycle degradation of ~0.008%. This work establishes a foundation for the molecular design and mechanism exploration of organic polymers with double-stranded ladder skeletons, which can be used to construct highly stable lithium metal batteries.

Introduction

One approach to decarbonization that appears attractive in the pursuit of net-zero emissions is electrification.[1–4] It is urgent to establish advanced high-energy-density storage systems for long-endurance unmanned aerial vehicles that can operate swiftly and buffer the flow of electricity from renewable energy sources to the grid.[5–8] As an anode material, lithium metal anodes (LMAs) have aroused widespread interest because of their unrivaled electrochemical properties, especially theoretical energy densities of more than 500 Wh kg^{-1}.[9–12] The high activity of lithium metal with most liquid electrolytes, however, makes it susceptible to the generation of an unreliable solid electrolyte interphase (SEI) at the interface of the Li anode.[13,14] Such an unstable SEI will continuously exhaust the electrolyte and lithium supply, leading to a pronounced reduction in Coulombic Efficiency (CE) and impeding the advancement of lithium metal batteries (LMBs).[15] Conversely, a stable and electronically insulating SEI is essential for protecting the lithium anode and suppressing dendrite growth. More specifically, the endurance of LMBs is determined to a large extent by the interfacial stabilization of the Li metal and the electrolyte, since the desolvation of Li^+ and composition of the SEI are the dominant ingredients driving the Li^+ migration kinetics and the deposition mode.[16–18] Currently, various strategies have been suggested to optimize the deposition of lithium metal, among which engineering of artificial protective layers is a more viable means, as this has been evidenced to have synergistic benefits, including rapid lithium ion delivery, isolation of electrolyte and lithium, elimination of lithium dendrite growth and electrode volume extension.[19]

At present, the majority of artificial protective layers still emphasize two points: suppressing dendrite growth through mechanical properties and isolating the sustained reaction involving Li metal with electrolyte, which has a limited contribution in adjusting the morphology of Li metal plating.[20–22] So far, covalent organic polymers (COPs) with tunable nanochannels and chemical modification have exhibited promising potential to modulate Li^+ diffusion and deposition behavior by covalently linking functionalized groups, in contrast to crystalline covalent organic frameworks (COFs), where structural rigidity limits adaptability to dynamic electrode interfaces.[23–26] It is noteworthy that rigid π-conjugated frameworks, such as covalent triazine frameworks (CTFs)[27–29] and graphitic carbon nitrides (g-C_3N_4),[30] have indeed been explored in LMBs.

Department of Chemical Engineering, School of Environmental and Chemical Engineering, Shanghai University, 99 Shangda Road, Shanghai 200444, China. E-mail: yongwang@shu.edu.cn

† These authors contributed equally to this work

However, while these materials are conjugated and contain nitrogen, their structures are typically two-dimensional sheets with a more heterogeneous distribution of interaction sites, which may not provide the uniform and well-defined ion transport pathways achievable in designed COP architectures. The chemical stability of the COPs is directly related to the bond strength of the organic linkage.[31] Therefore, sp^2c- and spc-linked COPs have improved chemical stability compared to other COPs owing to the higher bond energy of olefins and alkynyls, and hence exhibited good electrochemical performance.[18,32,33] Meanwhile, different linkages tend to have different properties, which can be attributed to their diversity in π-conjugation extent, planarity, and stability.[34,35] Ladder-type polymers are double-stranded or multi-stranded polymers with backbones linked by repeating ring units that share two or more atoms.[36–38] Ladder-type COPs with a more regular and symmetric molecular structure have received fewer investigations than ordinary COPs, which have been extensively researched. Although trapezoidal COPs were first proposed to overcome the problems of poor chemical stability and lack of intra-chip π-bonding in conventional COPs,[37,39–41] their application as a protective layer for LMAs has not been witnessed.

Herein, a novel kind of ladder-type phenazine-linked covalent organic polymers (denoted as PZ-CHPT) has been constructed with both completely aromatized and conjugated imine bonds in its framework, which serves as an artificial layer for LMAs. PZ-CHPT consists of two groups, phenazine (PZ, as an electron donor) and hexaazatriene (HAT, as an electron acceptor), thus expanding the delocalization of π-electrons and facilitating the migration of Li^+ through donor-acceptor interactions. Moreover, Li ions are capable of cation–π interaction with PZ-CHPT fragments (electron-rich aromatic compounds), optimizing ion transport through the pre-existing, relatively uniform molecular-level pores. These interactions promote lithium salt dissociation and immobilize anions *via* electrostatic effects, while reducing Li^+ diffusion barriers along the shortened intrinsic pathways to accelerate Li^+ transport. With these synergistic advantages, the PZ-CHPT compounds exhibit low solubility, high Li^+ transfer kinetics (transference number), enhanced mechanical strength, and interfacial stability, as inferred from theoretical calculations and experimental tests. Following 600 cycles at 1C, the PZ-CHPT-based full cells maintain an amazing 97.3% capacity, displaying a minor 0.0045% capacity degradation per cycle. Furthermore, the PZ-CHPT-modified symmetric cells demonstrate exceptional long-term cycling stability even after 1300 h cycling at 10 mA cm^{-2}. The combination of both strong ionic conductivity and outstanding mechanical qualities contributes to a stable SEI, which provides some insights into how the interface is tuned to stabilize LMAs.

Results and discussion

Molecular design principle and physicochemical configuration of ladder-type PZ-CHPT

As shown in Fig. 1a, the frameworks of PZ-CHPD and PZ-CHPT were constructed under solvothermal reaction conditions: cyclohexanehexaone (CHH-M), 1,2-phenylene diamine (PD-M) or 2,3,7,8-phenazinetetramine (PT-M), and all dissolved in a mixture of solvents under an Ar atmosphere (see the SI for more details). Initially, PZ-CHPT drew interest due to its completely extended 2D aromatic π-conjugated configuration, which offers a continuous pathway for electron/ion transfer through long-distance π–π stacking and orbital overlap. In phenazine fragments, the electronegative nitrogen (N) atoms polarize adjacent *σ*-bonds, while their p-orbital lone pairs participate in π-conjugation, collectively redistributing electron density across the aromatic framework to facilitate charge transfer. Inspired by the above theories, it is believed that incorporating functional groups such as phenazine (PZ) and hexaazatriene (HAT) into the backbone will prolong the planar structure (π-conjugation) and promote stability. Indeed, the high quadrupole moment of HAT can endow PZ-CHPT with more negative potential and serve as the fundamental core of ladder-type COPs, which are mainly concentrated around highly symmetric hexaketocyclohexane, as revealed by the simulated molecular *trans*-electrostatic potential (ESP, Fig. S1).[37,39–41] Cation–π interactions, which arise from the electrostatic attraction between cations and the electron-rich π systems of aromatic compounds, are recognized as one of the strongest non-covalent forces and hold great potential for enhancing Li^+ transport.[42–45] Furthermore, the fully aromatic conjugated imine bond present in PZ-CHPT is strengthened by the sharing of two N atoms connected to a periodically repeating ring unit (Fig. 1b). Based on these characteristics, PZ-CHPT features relatively uniform molecular-level pores with functionalities that scatter Li^+ through cation–π interactions, shorten their transport pathways, and aid the rapid migration of Li^+ (Fig. 1c).

The morphology of PZ-CHPD and PZ-CHPT was disclosed by scanning electron microscopy (SEM) and transmission electron microscopy (TEM). SEM (Fig. 2a and b) and TEM (Fig. 2c) images of PZ-CHPD reveal an aggregated ribbon-like appearance with a diameter of ∼200.0 nm, and the C and N elements are uniformly distributed across PZ-CHPD (Fig. S2). For the PZ-CHPT sample, rod-like structures with a diameter of ∼30 nm were also observed, which appeared as a daisy-like sphere made of stacked nanorods (Fig. 2d–f). Furthermore, the C and N elements, with the mass content of 82.5% and 17.5% (Fig. S3), are dispersed equally across the entire products, as shown by the corresponding elemental mapping images (Fig. 2g–i). As depicted in Fig. 2j and k, the height variation across the protrusion area is less than 10.6 nm on average, demonstrating the smooth and uniform surface of PZ-CHPT. Moreover, the surface of PZ-CHPT manifests a high Young's modulus value of 8.9 GPa, which helps suppress the formation of Li dendrites (Fig. 2l).

Fourier transform infrared (FT-IR) spectroscopy and Raman spectroscopy confirmed the chemical cross-linking and the formation of the desired network structure in PZ-CHPT. The FT-IR spectra of CHH-M, PT-M and PD-M reveal active groups such as amino and carbonyl, indicated by N–H stretching vibrations ∼3450 cm^{-1} and C=O stretching vibrations in the region of 1640 cm^{-1} (Fig. S4). Additionally, the FT-IR spectra of PZ-CHPD and PZ-CHPT display strong characteristic signals at 1280 cm^{-1}, attributed to the generation of phenazine linkages (C–C=N–C)

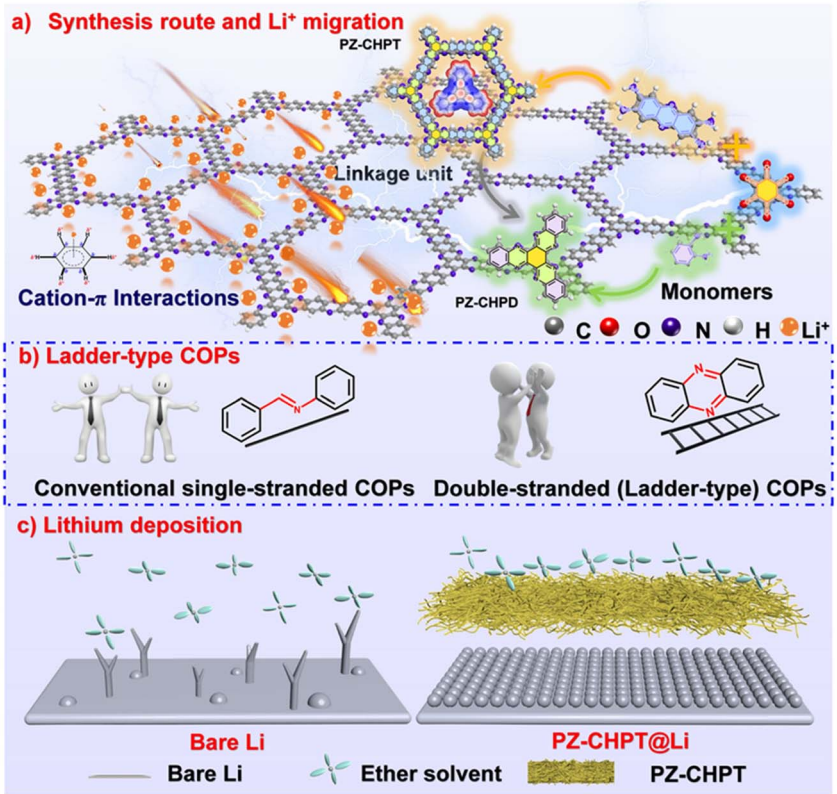

Fig. 1 Schematic illustration of the structural design and mechanism of PZ-CHPT. (a) Fabrication process and the Li^+ migration mechanism for the PZ-CHPT protective layer. (b) Double-stranded (ladder-type) COPs. (c) Morphology evolution during the deposition on bare Li and Li@PZ-CHPT.

(Fig. S5).[46] Additional evidence of the functional linkages in PZ-CHPD and PZ-CHPT was obtained from Raman spectra, which display distinctive peaks at 1210 cm^{-1} and 1235 cm^{-1}, respectively, and are approximately consistent with the above FT-IR results (Fig. S6).[47] Moreover, the powder X-ray diffraction (XRD, Fig. S7) profiles reveal that PZ-CHPD and PZ-CHPT possess fairly regularly ordered structures arising from π–π stacking of individual phenazine derivative molecules, which is further confirmed by the peaks at 291.3 eV and 290.0 eV observed in the high-resolution C 1s XPS spectra, respectively (Fig. S8e).[48] Furthermore, N_2 isothermal adsorption–desorption measurements were performed to assess the changes in pore properties before and after extending the π-conjugation.[49] On the basis of the results, the sorption curves of PZ-CHPD and PZ-CHPT are both of type IV with the hysteresis loops of type H3, indicating the presence of mesopores. The Brunauer–Emmett–Teller surface areas (S_{BET}) of PZ-CHPD and PZ-CHPT were also determined to be 36.2 and 59.2 $m^2\ g^{-1}$, respectively (Fig. S9). It is suggested that the migration of Li^+ may be mainly guided by the chemical effect rather than simple physical adsorption.[50,51] The relatively higher S_{BET} (compared to PZ-CHPD) and intrinsic conjugated porous structure of PZ-CHPT allow for optimal use of lithiophilic sites, suggesting the potential for a highly stable interface. Additionally, thermogravimetric analysis (TGA) was also carried out to confirm the thermal endurance of the as-synthesized PZ-CHPD and PZ-CHPT. As the temperature increases to 800 °C, PZ-CHPT exhibits significantly lower weight loss compared to PZ-CHPD, indicating superior thermostability of the formed extensive π-conjugated frameworks (Fig. S10).[52] Furthermore, comparison experiments on solubility in ether-based electrolyte also confirm that PZ-CHPT exhibits significantly higher insolubility than the relatively small molecule of PZ-CHPD (Fig. S11).

Long-term performance evaluation of cells assembled with ladder-type PZ-CHPT

Due to the enriched C and N atoms present in the enlarged π system of PZ and HAT, which serve as rigid heterocyclic units to strengthen the covalent linkages, the resulting PZ-CHPT is expected to be lithiophilic and capable of regulating the diffusion behavior of Li^+. To examine the Li plating and stripping properties, half-cells were cycled at a current density of 0.5 mA cm^{-2} and capacity of 1 mAh cm^{-2}, as plotted in Fig. 3a. The Li||PZ-CHPT@Cu half-cell demonstrated stable cycling, with a high CE of 98.7% over 415 cycles, while the Li||PZ-CHPD@Cu cell failed after 97 cycles, with a CE of less than 63.9% after 103 cycles. At 1 mA cm^{-2}/1 mAh cm^{-2} (Fig. 3b), the Li||PZ-CHPT@Cu half-cell achieved 330 cycles, outperforming the Li||PZ-CHPD@Cu cell, which lasted for only 140 cycles. Furthermore, voltage–time curves (Fig. 3c) show that the Li||PZ-CHPT@Cu cell maintained a stable platform voltage (58.2 mV

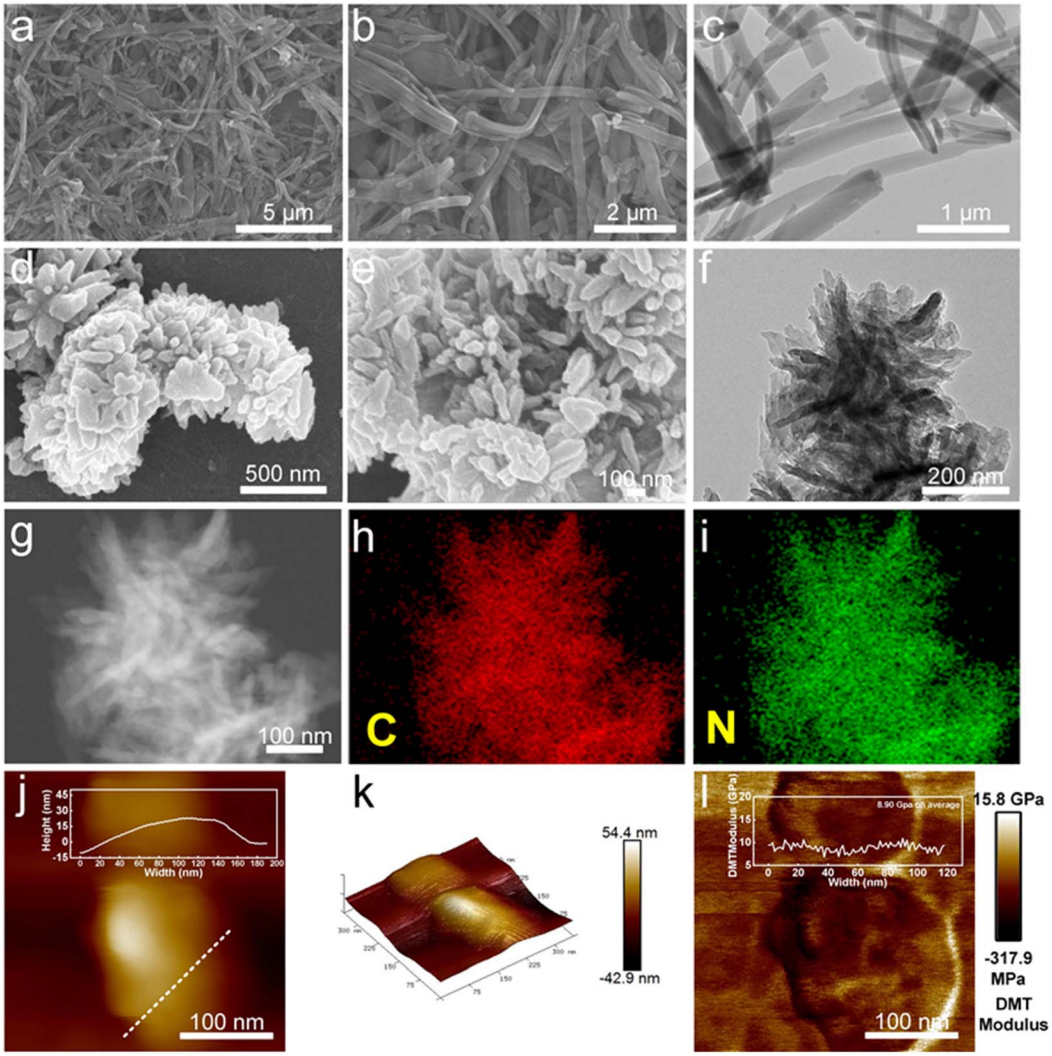

Fig. 2 Structural characterization studies of PZ-CHPT. SEM images of (a and b) PZ-CHPD and (d and e) PZ-CHPT. TEM images of (c) PZ-CHPD and (f) PZ-CHPT. (g–i) EDS analysis mapping images of PZ-CHPT. (j) AFM image, (k) 3D AFM image and (l) elastic modulus mapping of the top surface of PZ-CHPT.

initially, 66.2 mV after 300 cycles), indicating minimal damage to the SEI layer.

Unfortunately, as depicted in Fig. 3d, the asymmetric cells with Li‖PZ-CHPD@Cu experienced tangible voltage fluctuations for the initial 50 cycles, due to the SEI cracking and Li dendrite formation. The aggregation of anions at the anode during the discharging process, which impairs battery performance, highlights the Li^+ transference number (t_{Li^+}) as a primary metric for quantitatively assessing single-ion migration competence of PZ-CHPT. It is indicated that the t_{Li^+} value of PZ-CHPT is 0.74 (Fig. S12a), which is significantly higher than that of PZ-CHPD (0.47, Fig. S12b). Such consequences firmly endorse the high ion selectivity of the PZ-CHPT protective layer with an extended aromatic π-conjugated system for Li^+, which contributes to alleviating concentration polarization and inhibiting interfacial side reactions.

To ulteriorly evaluate the voltage hysteresis (VH) and cycle stability during extended galvanostatic charge/discharge cycles, symmetric cells were constructed with PZ-CHPD and PZ-CHPT as the working electrodes. As demonstrated in Fig. 3e, symmetric cells with PZ-CHPT manifested a low voltage hysteresis (VH) of 23.5 mV and stable cycling over 3200 h at 3 mA cm^{-2}, whereas PZ-CHPD cells experienced a significant voltage rise after 700 h. More importantly, the cycling stability of PZ-CHPT-modified symmetric cells at a high current density of 5 mA cm^{-2} was also evaluated, as disclosed in Fig. 3f. Notably, it conveys that PZ-CHPT-modified symmetric cells preserve a steady voltage profile for over 2800 h (VH ~32.4 mV), whereas batteries protected by PZ-CHPD can only tolerate up to 500 h as a consequence of the formation of a possible thick SEI layer and are not even operable for repeated operation at 10 mA cm^{-2}. Comparatively speaking, the PZ-CHPT cells continue to function for 1300 h at 10 mA cm^{-2} with an overpotential of ~43.8 mV, demonstrating their ability to withstand harsh current conditions (Fig. 3g–h). In brief, this implies that PZ-CHPT-modified LMAs are capable of exhibiting lower VH and

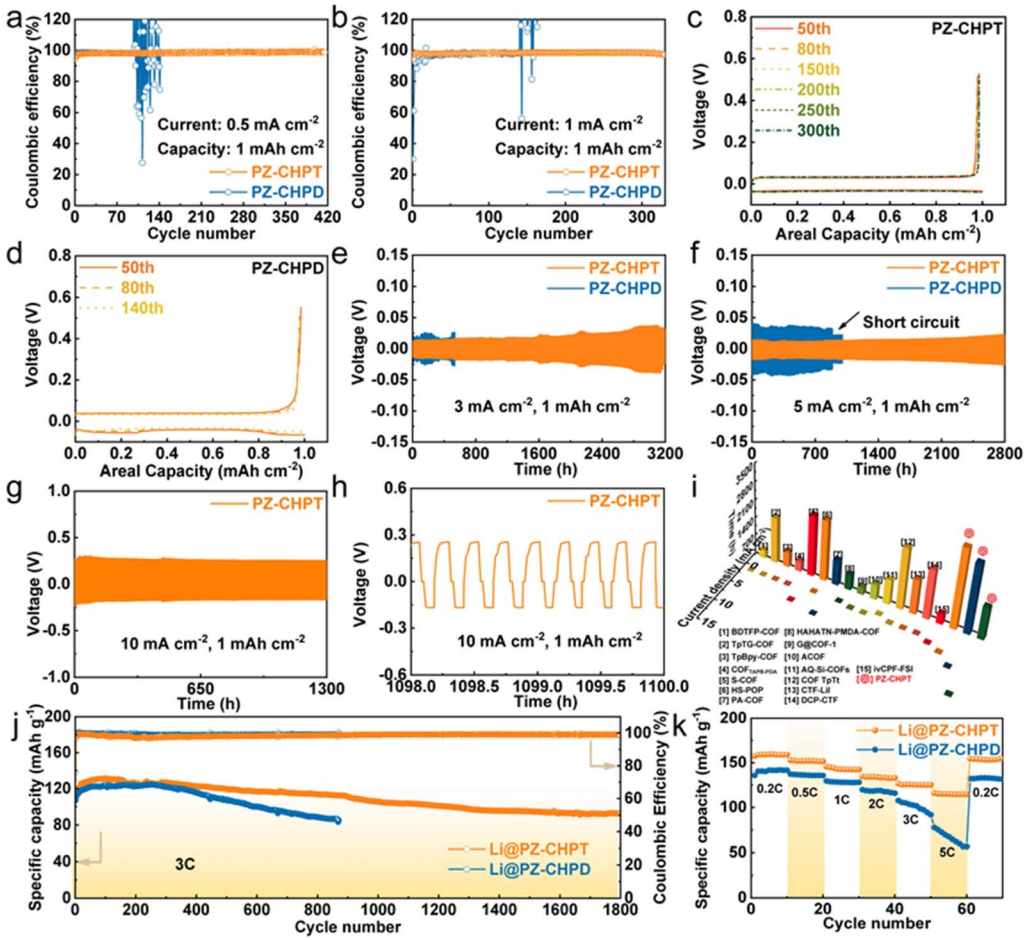

Fig. 3 Electrochemical properties of PZ-CHPD in comparison to PZ-CHPT. CE of the Li||PZ-CHPD@Cu and Li||PZ-CHPT@Cu half cells operated at (a) 0.5 mA cm^{-2} and (b) 1 mA cm^{-2}. Galvanostatic voltage curves of (c) Li||PZ-CHPT@Cu and (d) Li||PZ-CHPD@Cu half cells. Long-term cycling performance in symmetric cells containing Li@PZ-CHPD||Li@PZ-CHPD and Li@PZ-CHPT||Li@PZ-CHPT at (e) 3 mA cm^{-2}, 1 mAh cm^{-2}, (f) 5 mA cm^{-2}, 1 mAh cm^{-2} and (g) 10 mA cm^{-2}, 1 mAh cm^{-2}. (h) The corresponding voltage–time curves of 10 mA cm^{-2}, 1 mAh cm^{-2}. (i) Evaluation of the deposition/stripping life with previous relative COPs. (j) Long-term cycling stability and k) rate properties of the Li@PZ-CHPD|LFP and Li@PZ-CHPT|LFP full batteries.

more consistent cycling than PZ-CHPD-modified symmetric cells. These good long-cycle performances are outstanding among previous relative reports using COPs.[53–67] (Fig. 3i and Table S1).

In light of the extraordinary Li^+ migration and dendrite inhibition characteristics of PZ-CHPT, we have further pursued its feasibility for full batteries incorporating $LiFePO_4$ (LFP) cathodes. As forecasted, the Li@PZ-CHPT electrode outperforms the Li@PZ-CHPD electrode with regard to long-term stability. It is important to highlight that, even after 600 cycles at 1C, the Li@PZ-CHPT||LFP cell retains a capacity of 124.3 mAh g^{-1} (~97.3% capacity retention) and 99.2% CE (Fig. S13–S15), demonstrating efficient Li^+ transport regulation by PZ-CHPT. In contrast, the Li@PZ-CHPD||LFP full cell retains only 82.1% capacity and 99.0% CE after 360 cycles, primarily caused by ongoing SEI disruption and active Li depletion. Even at a higher current rate of 3C, the Li@PZ-CHPT||LFP full cell retains 86.1% capacity (92.1 mAh g^{-1}) and high CE (~99.1%) after 1800 cycles, demonstrating remarkable high-rate cycling durability (Fig. 3j). However, the Li@PZ-CHPD||LFP cell reveals poorer performance with a capacity of 85.0 mAh g^{-1} and a relatively low capacity retention (79.2%) after 870 cycles, followed by rapid degradation due to increased overpotential (from the 400th cycle (112.3 mV) to the 870th cycle (208.6 mV), Fig. S16). Additional full-cell tests with high mass loading (~12 mg cm^{-2}) and thin lithium anodes (~150 μm) have been conducted, with results shown in Fig. S17, confirming that the Li@PZ-CHPT||LFP full cells achieved a discharge capacity of 140.1 mAh g^{-1} at 3C and retained 78.7% capacity after 500 cycles, robustly demonstrating the stabilization of the lithium anode interface by the PZ-CHPT layer under practical conditions. The outstanding cycling performances of the Li@PZ-CHPT||LFP full cell confirm that the artificial interface protection layer contains numerous lithiophilic units (C–C=N–C linkages, C=N units, and aromatic rings), promoting uniform lithium metal deposition. From the results reflected in Fig. 3k, the Li@PZ-CHPT||LFP cell demonstrated excellent rate performance and cycling stability, apparently outperforming Li@PZ-CHPD||LFP

across different cycling rates. Upon returning to 0.2C, the Li@PZ-CHPT||LFP cell retained an average reversible capacity of 153.9 mAh g^{-1} while sustaining similar capacities in consecutive cycles, suggesting efficient Li^+ transfer through PZ-CHPT segments.[68] To investigate the reaction kinetics throughout the charge/discharge cycle, EIS measurements were conducted on the Li@PZ-CHPT||LFP full cell, with the impedance at different states of charge displayed in Fig. S18. The minimal changes observed during cycling indicate a stable interface and homogeneous Li^+ flux, directly supporting the role of PZ-CHPT's micropores in creating regulated Li^+ migration pathways.

Structural evolution and mechanism of ladder-type PZ-CHPT

To intuitively disclose the effect of PZ-CHPT on boosting homogeneous Li^+ flow and refining Li electroplating behaviors, SEM analysis was implemented to study the surface evolution of lithium electrodes shielded by PZ-CHPT. As exemplified in Fig. S19, the bare Li anode exhibits a loose, fluffy structure after cycling, along with an increased amount of lithium dendrite. After the 1st cycle (Fig. 4a) in the ether-based electrolyte, the Li@PZ-CHPD anode surface develops uneven Li depositions that act as charge centers for the tip effect, increasing dendritic growth while inhibiting Li^+ flux and encouraging dendrite formation. After the 100th cycle (Fig. 4b), there is a large number of unwanted block-like protrusions with uneven shape. However, the Li@PZ-CHPT anode exhibits a reasonably flat and homogeneous surface morphology without dendrites throughout cycling (Fig. 4c and d), confirming that the PZ-CHPT protective layer ensures a stable interface on the Li anode. AFM images further validate the results, with the AFM analysis revealing distinct surface geometry distributions between the Li@PZ-CHPD and Li@PZ-CHPT anodes. The three-dimensional (3D) AFM scanning images in Fig. $4c_1$–d_1 reveal that the surface morphology of the cycled Li@PZ-CHPT is substantially smoother than Li@PZ-CHPD in Fig. $4a_1$–b_1, suggesting its innate resilience to the repeated Li metal stripping/plating.

Moreover, the Li@PZ-CHPT buffer layer yielded an average high Young's modulus of ~10.7 GPa (Fig. 4g and h), as confirmed by AFM nano-indentation analysis (Fig. S20), which is substantially larger than the threshold value (~6 GPa) required to hinder dendritic Li development, according to earlier studies.[69,70] It is indicated that the nitrogen-enriched PZ-CHPT interface layer can spontaneously generate a highly polar Li–N SEI protective layer through the interaction between Li metal and the N-rich atoms over the course of cycling, thereby improving the rigidity of the interface. The reduced modulus of the SEI (~6.4 GPa, Fig. 4e and f) on Li@PZ-CHPD compared to PZ-CHPT after Li deposition and limited dendrite inhibition effect can be attributed to the uneven plating process, which causes the SEI to break and leads to more severe side interfacial reactions. After initial plating, compactly-stacked Li grains were consistently deposited under the Li@PZ-CHPT surface (Fig. 4i), suggesting the significant function of the enlarged π system, multifunctional functional groups (C–C=N–C linkages, C=N units, and aromatic rings) and additional cation–π interactions in regulating Li deposition. As outlined in Fig. S21, the thickness of the PZ-CHPT layer is approximately 9.6 μm in this work. Likewise, as a result of structural evolution during the 100th cycle (Fig. 4j), the Li@PZ-CHPT electrode retains a flat and compact surface, which boosts CE and cycling stability. In contrast to Li@PZ-CHPT, the cross-section of Li@PZ-CHPD in the ether-type electrolyte (Fig. 4k) validates that the Li anode appears severely corroded after the 1st cycle with an uneven surface. A substantial amount of fluffy Li accumulates along the vertical direction of the substrate after the 100th cycle (Fig. 4l) in the case of the Li@PZ-CHPD layer with insufficient effect, authenticating inhomogeneous Li plating and dendrite growth.

To gain an in-depth overview of the inhibitory action of the Li@PZ-CHPT anode on Li dendrite formation, an optical microscope (OM) was used to monitor *in situ* Li deposition in a non-pressured Li//Li electrolytic cell at 3 mA cm^{-2} with various protective layers. The outermost layer of bare Li foil (Fig. S22) is coarse, and its leading edge is tiny, which results in unequal charge distribution and ion movement. After 10 min of electroplating, mossy Li grows on the edge and surface, indicating uneven galvanization, and these protrusions evolve into uncontrolled dendrites during the next plating step. The Li@PZ-CHPT anode, on the other hand, exhibits no significant protrusions or dendrites during the plating procedure (Fig. 4m). Due to the poorer lithiophilic and chemodynamical stability of the Li@PZ-CHPD anode, considerable dendritic development along the edges and visible discoloration from dissolution are observed (Fig. S23). To gain a deeper understanding of how Li^+ diffusion is influenced by the PZ-CHPT network, we additionally conducted simulations of Li^+ desolvation. Fig. 5a indicates that PZ-CHPT has a lower unoccupied molecular orbital (LUMO) energy value (−4.553 eV) than PZ-CHPD (−3.832 eV), indicating a better electron affinity. The energy gaps (ΔE) between the highest occupied molecular orbital (HOMO) and LUMO for PZ-CHPT and PZ-CHPD were found to be 2.072 and 2.243 eV, respectively. As anticipated, PZ-CHPT exhibits a higher redox potential than PZ-CHPD, attributed to its enlarged ladder-type conjugated polymeric skeleton structure with high molecular polarizability, which results in better electrical conductivity for rapid electron transmission.[41,71]

Consequently, DFT simulations were used to explore the interaction strength of Li ions or lithium bis(trifluoromethanesulfonyl)imide (LiTFSI) with solvents, as well as with PZ-CHPT. The adsorption energy of Li^+ with the corresponding species takes the following order, as shown in Fig. 5b: PZ-CHPT (−1.624 eV) > $TFSI^-$ (−1.277 eV) > PZ-CHPD (−0.69 eV) > DME (−0.513 eV) > DOL (−0.499 eV). In detail, the interaction between Li^+ and PZ-CHPT (−1.624 eV) is stronger than that with $TFSI^-$ (−1.277 eV), suggesting that PZ-CHPT can facilitate Li^+ dissociation from solvent clusters, expedite the adsorption on the enriched nitrogen (N) sites, and enhance its concentration within the 1D nanochannels. This is primarily because the fully arylated PZ-CHPT has a ladder-type coplanar polymeric skeleton with low intrachain torsional disorder. Not surprisingly, this contributes to a lower migration energy barrier by reducing the energy consumption of Li^+ during diffusion and increasing π-electron delocalization, which facilitates the exertion of Li^+ and the aromatic rings through cation–π interactions.

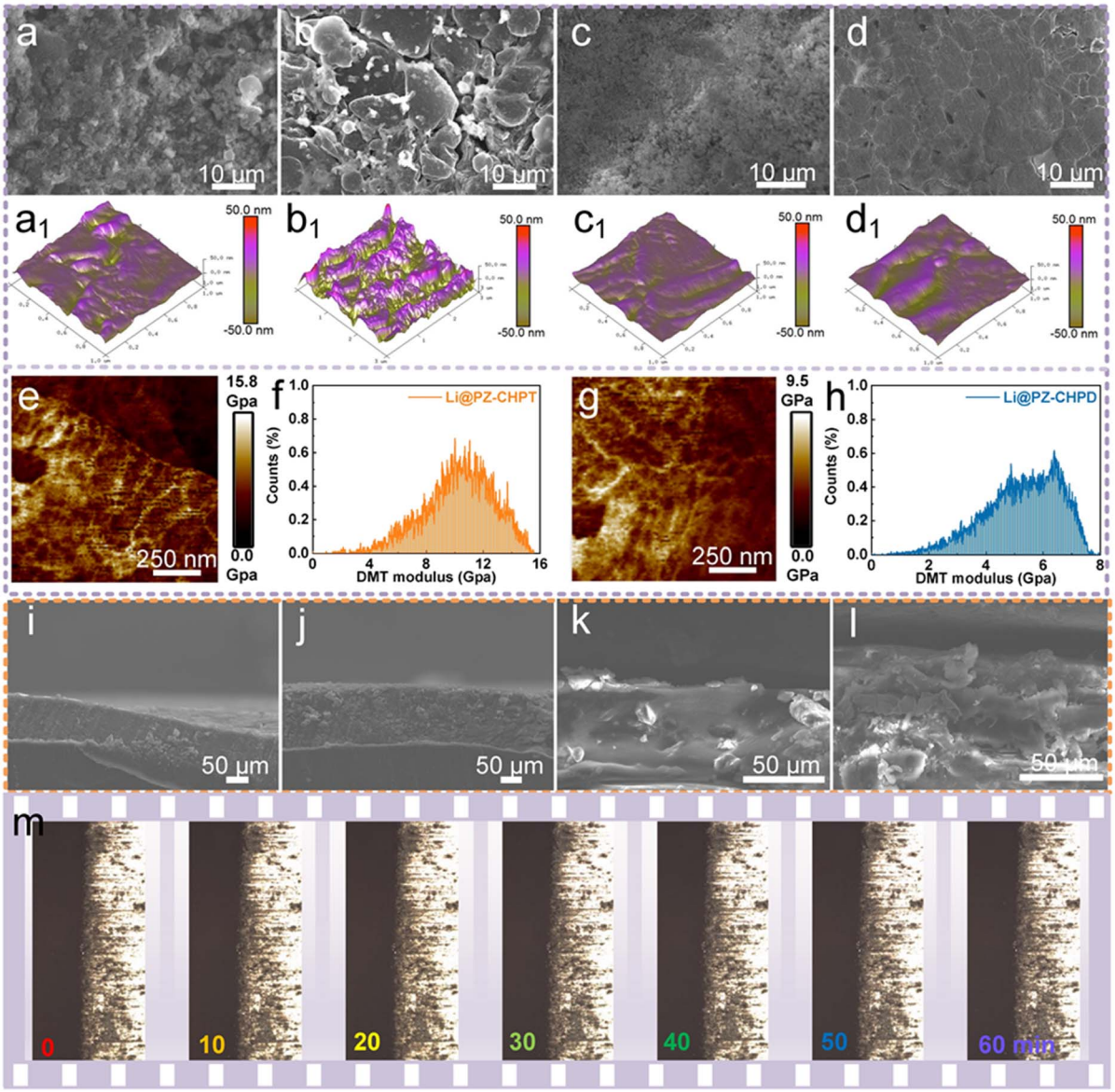

Fig. 4 Effects of the PZ-CHPT interphase on Li deposition/stripping chemistry. SEM images of the Li@PZ-CHPD anode after (a) the 1st cycle and (b) the 100th cycle and the Li@PZ-CHPT anode after (c) the 1st cycle and (d) the 100th cycle. The corresponding AFM images of the Li@PZ-CHPD anode after (a_1) the 1st cycle and (b_1) the 100th cycle and the Li@PZ-CHPT anode after (c_1) the 1st cycle and (d_1) the 100th cycle. The Young's modulus of (e) Li@PZ-CHPT and (g) Li@PZ-CHPD anodes. The Young's modulus histogram of (f) Li@PZ-CHPT and (h) Li@PZ-CHPD anodes. Cross-sectional SEM images of the Li@PZ-CHPT anode after (i) the 1st cycle and (j) the 100th cycle and the Li@PZ-CHPD anode after (k) the 1st cycle and (l) the 100th cycle. (m) *In situ* OM images of Li deposition on PZ-CHPT.

Considering the DFT calculations discussed above, it can be concluded that under such a high Li^+ affinity capability, Li^+ would readily desolvate and dissociate, causing Li^+ to migrate quickly.

As a further step, to investigate the unique interaction mechanism between PZ-CHPT and Li and examine its Li deposition phenomena, *in situ* Raman spectra (Fig. 5c) were simultaneously recorded during the entire process (discharging–plating–charging process) of PZ-CHPT-based asymmetric batteries. In the early stages, signature peaks corresponding to C=N units (~1528 cm^{-1}), C–C=N–C linkages (~1200 cm^{-1}), and aromatic rings (~1460, 1285, and 605 cm^{-1}) were captured, as depicted in the right part of Fig. 5c.[47] The attenuation of C=N and aromatic ring signals during discharging, followed by recovery during charging, revealed reversible Li coordination at C=N lithium-affinity sites and cation–π interactions with conjugated π-electrons, respectively.[72] Intriguingly, the peak (~605 cm^{-1}) is also attributed to vibrations in the low-frequency region of the aromatic rings, imputed to the stronger π–π interactions for the fully extended 2D aromatic π-conjugated PZ-CHPT, which is in agreement with the XPS findings (Fig. S8b). The C–C=N–C vibrational peak (~1200 cm^{-1}) exhibited a gradual intensity reduction during discharge followed by restored intensity upon charging,

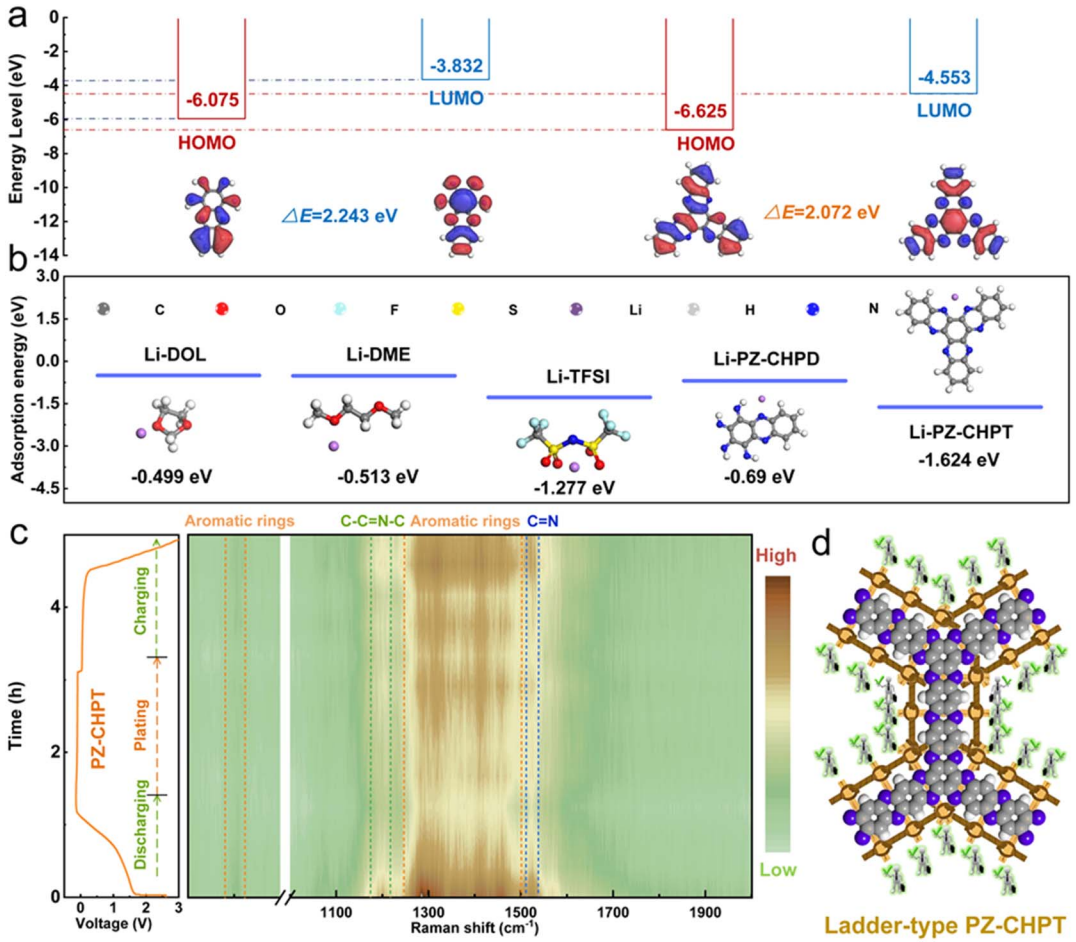

Fig. 5 The Li^+ transport mechanism in PZ-CHPT. (a) Diagram of the LUMO and HOMO energy levels and the corresponding optimized geometrical structures of PZ-CHPT and PZ-CHPD. (b) The configurations and corresponding binding energies of Li^+ with PZ-CHPD, PZ-CHPT and LiTFSI-based electrolyte. (c) *In situ* Raman measurements and the associated voltage–time plots for Li@PZ-CHPT. (d) Schematic illustration of Li^+ interaction with ladder-type PZ-CHPT.

indicating reversible Li^+ coordination with C–C=N–C linkages during cycling. Raman spectroscopy, through spatial localization, measures molecular vibrational frequencies, enabling the lateral observation of lithium deposition *via* the attenuation of specific peaks.[73] As anticipated, no significant changes are observed in the strength of the C–C=N–C linkages, C=N units, and aromatic rings during lithium deposition process, suggesting the stability of the PZ-CHPT protective layer and indicating that Li is mainly deposited beneath it, which aligns with the *in situ* OM results (as illustrated in Fig. 4m), as well as with prior studies.[74–76] The double-stranded ladder framework of PZ-CHPT, constructed through periodic repetition of N-bridged units, features a rigid backbone and extended π-conjugation. This architecture enables two synergistic ion-transport mechanisms: (1) intramolecular cation–π interactions between Li^+ and electron-rich motifs dynamically polarize π-electron clouds to guide Li^+ hopping along conjugated chains; (2) intermolecular π–π stacking creates relatively ordered nanochannels that provide continuous diffusion pathways, collectively facilitating rapid Li^+ migration, as visualized in Fig. 5d.

An *in situ* FT-IR spectroscopy system was constructed to delineate the ability of the PZ-CHPT layer to mitigate electrolyte degradation and suppress side reactions, using a symmetric cell with Li electrodes (with PZ-CHPD or PZ-CHPT coating modification). By illuminating the ether-based electrolyte with IR light, the *in situ* FT-IR spectra of PZ-CHPD reveal characteristic peaks with downward trends, which indicate the diminishment of the original functional groups. Compared to the Li@PZ-CHPD electrode (Fig. S24), the Li@PZ-CHPT electrode (Fig. S25) demonstrates much lower voltage polarization. In the FT-IR spectra, the transmission peaks at ~887 cm^{-1} are indicative of the $TFSI^-$ groups, while signals at ~1352, 1183 and 1055 cm^{-1} are assigned to the S=O, C–O, and C–F groups, respectively.[29]

Over extended cycling periods (3D image in Fig. 6a), the $TFSI^-$ peaks diminish, whereas the peaks for S=O, C–F and C–O become more pronounced, and no peaks revert to their original state, signifying the irreversible depletion of the electrolyte. In contrast, there are negligible changes in these four peaks for the Li@PZ-CHPT electrode (3D image in Fig. 6b), implying that side reactions with the electrolytes are minimal.

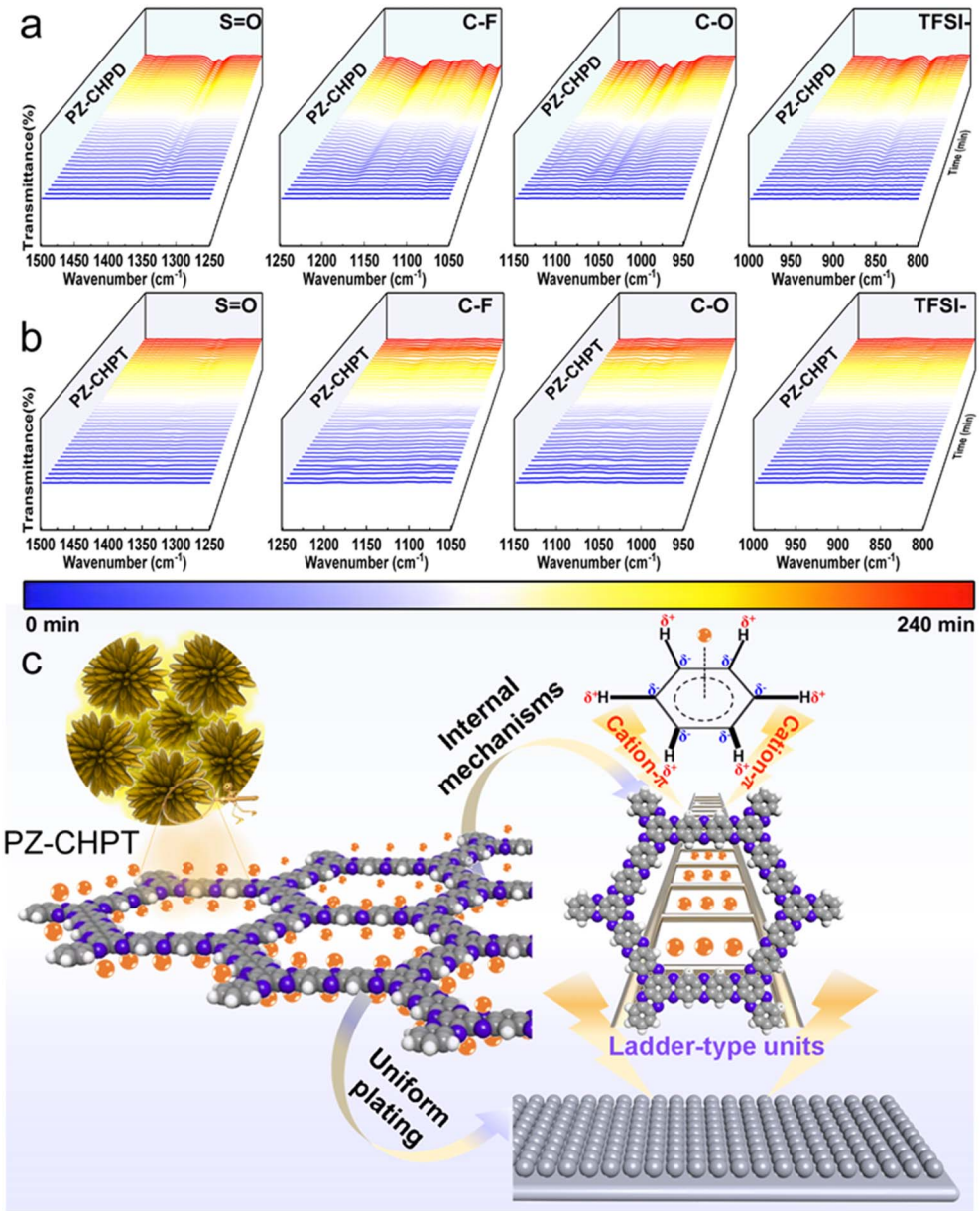

Fig. 6 *In situ* FT-IR analysis of electrolyte consumption in (a) PZ-CHPD and (b) PZ-CHPT modified Li symmetric cells. (c) The mechanism explanation of the PZ-CHPT film in enhancing Li^+ desolvation, migration, and the Li deposition process.

Taking into account the theoretical insights and experimental observations, the proposed origin and mechanism for Li^+ migration within the PZ-CHPT interfacial layer are summarized in Fig. 6c. First, gradient polarization or electrostatic attraction drives the solvated Li to swim in the direction of the adjacent PZ-CHPT modified surface during the first discharge procedure. Second, because of the strong competition between Li and the solvent molecules and the presence of ultra-homogeneous distributed lithiophilic sites (C–C═N–C linkages, C═N units, and aromatic rings), cation–π interactions are stimulated, and Li^+ may momentarily separate from its solvation shell and adsorb directly onto the PZ-CHPT coating layer. Simultaneously, the spatially limited and negatively charged nanopores resist the infiltration and diffusion of anions, which is believed to play an important part in curbing electrolyte decomposition. It is worth noting that the extended π-conjugation in the fully π-conjugated ladder-type PZ-CHPT allows electron clouds to delocalize continuously along the polymer backbone, greatly promoting the diffusion and movement of Li^+.

Conclusions

In conclusion, a ladder-type phenazine-linked covalent organic polymer (PZ-CHPT) was designed to strategically control Li^+ transport behaviors and interfacial charge distribution, aiming at enhancing the electrochemical performances of LMBs. PZ-CHPT with a fully extended 2D aromatic π-conjugated system

features a rigid heterocyclic unit that reduces intra-chain torsional disorder and strengthens covalent bonding, as well as a highly uniform distribution of nitrogen-rich sites that enhance affinity for Li^+. These structural characteristics, combined with localized micropores that create segregated Li^+ migration pathways, act as a Li^+ conduction splitter, governing kinetically-enhanced Li^+ migration and desolvation. Leveraging these synergistic properties, the PZ-CHPT compounds show negligible solubility in the electrolyte, high Li^+ transfer kinetics ($t_{Li^+} = 0.74$), enhanced mechanical strength (Young's modulus ~10.7 GPa after cycling), and excellent interfacial stability (with 86.1% capacity retention after 1800 cycles), as supported by theoretical predictions and various experimental probing techniques. This work provides insights for the molecular design and mechanism exploration of ASEIs based on COPs with double-chain-linked ladder skeletons, which could be applied in the development of highly stable LMBs.

Author contributions

Xiao-Meng Lu and Haichao Wang: conceptualization, data curation, formal analysis, investigation, methodology, writing – original draft; Yiwen Sun and Yi Xu: data curation, formal analysis, investigation, validation; Yang Wu, Weiwei Sun, Chao Yang and Yifan Zhang: data curation, formal analysis, validation, writing – review & editing; Yong Wang: conceptualization, funding acquisition, project administration, resources, supervision, validation, writing – review & editing.

Conflicts of interest

There are no conflicts to declare.

Data availability

All the data supporting this article have been included in the main text and the supplementary information (SI). Supplementary information: experimental section, detailing the synthetic protocols, alongside the characterization methodologies and electrochemical cell assembly procedures; supplementary figures, which include computational ESP maps, morphological and elemental analyses (SEM, EDS, EDX), structural and chemical state characterizations (FT-IR, Raman, PXRD, XPS), porosity evaluations (BET), thermal stability profiles (TGA), electrolyte solubility tests, comprehensive electrochemical performance data. See DOI: **https://doi.org/10.1039/d5sc06777d**.

Acknowledgements

We gratefully appreciate the National Natural Science Foundation of China (92472107) and the Innovative research team of high-level local university in Shanghai for their financial support.

Notes and references

1 B. C. Gibb, The Rise and Rise of Lithium, *Nat. Chem.*, 2021, **13**, 107–109.
2 S. Chu, Y. Cui and N. Liu, The Path towards Sustainable Energy, *Nat. Mater.*, 2017, **16**, 16–22.
3 T. Liu, X.-M. Lu, S. Lu, R. Jiang, M. Guo, C. Guo, Z. Yu and Y. Wang, Hierarchical hollow nanospheres of imine-based covalent organic frameworks with built-in Ag sites for fast-charging lithium metal batteries, *Chem. Sci.*, 2025, **16**, 17725–17735.
4 H. Wang, X.-M. Lu, Y. Sun, Y. Xu, W. Sun, L. Lv, S. Chen and Y. Wang, Intramolecular Dual Donor-Acceptor Featured Covalent Organic Frameworks Enabled by Gating Effects for Ultra-Stable Na-Metal Batteries, *Angew. Chem., Int. Ed.*, 2025, **64**, e202508503.
5 J. Chang, Q. Y. Huang, Y. Gao and Z. J. Zheng, Pathways of Developing High-Energy-Density Flexible Lithium Batteries, *Adv. Mater.*, 2021, **33**, 2004419.
6 C. F. Guo, T. C. Liu, Z. Z. Wang, Y. X. Wang, M. Steven, Y. H. Luo, X. P. Luo and Y. Wang, Regulating the Spin-State of Cobalt in Three-Dimensional Covalent Organic Frameworks for High-Performance Sodium-Iodine Rechargeable Batteries, *Angew. Chem., Int. Ed.*, 2024, **64**, e202415759.
7 J. Ding, J. J. He, L. Chen, Y. Sun, Y. Xu, L. P. Lv and Y. Wang, Zincophilic Sites Enriched Hydrogen-Bonded Organic Framework as Multifunctional Regulating Interfacial Layers for Stable Zinc Metal Batteries, *Angew. Chem., Int. Ed.*, 2025, **64**, e202416271.
8 X.-M. Lu, J. Aslam, M. A. Waseem, Y. Zhang, W. Sun and Y. Wang, Harnessing interfacial engineering in covalent organic frameworks for lithium metal batteries, *Coord. Chem. Rev.*, 2025, **535**, 216604.
9 Y. L. Chen, Z. Yu, P. Rudnicki, H. X. Gong, Z. J. Huang, S. C. Kim, J. C. Lai, X. Kong, J. Qin, Y. Cui and Z. N. Bao, Steric Effect Tuned Ion Solvation Enabling Stable Cycling of High-Voltage Lithium Metal Battery, *J. Am. Chem. Soc.*, 2021, **143**, 18703–18713.
10 Y. N. Cao, Y. Sun, C. F. Guo, W. W. Sun, Y. Wu, Y. Xu, T. C. Liu and Y. Wang, Dendritic sp Carbon-Conjugated Benzothiadiazole-Based Polymers with Synergistic Multi-Active Groups for High-Performance Lithium Organic Batteries, *Angew. Chem., Int. Ed*, 2024, **63**, e202316208.
11 S. Wu, X. Lu, Y. Sun, H. Wang, M. A. Waseem, J. Aslam, Y. Xu, L.-P. Lv and Y. Wang, Hydrogen-Bonded Organic Framework with Desolventization and Lithium-Rich Sites for High-Performance Lithium Metal Anodes, *Angew. Chem., Int. Ed.*, 2025, **64**, e202506892.
12 J. Aslam, M. A. Waseem, Y. B. Wu, W. W. Sun and Y. Wang, Recent developments in covalent Triazine frameworks for Lithium-ion and Lithium–sulfur batteries, *Adv. Colloid Interface Sci.*, 2025, **341**, 103479.
13 P. B. Zhai, L. X. Liu, X. K. Gu, T. S. Wang and Y. J. Gong, Interface Engineering for Lithium Metal Anodes in Liquid Electrolyte, *Adv. Energy Mater.*, 2020, **10**, 2001257.

14 J. Aslam, M. A. Waseem, X. M. Lu, S. L. Wu, W. W. Sun and Y. Wang, MXene-Infused Anode Architectures for Lithium Metal Batteries: Pioneering Strategies to Address Core Limitations, *Small*, 2025, 21.

15 H. P. Wu, H. Jia, C. M. Wang, J. G. Zhang and W. Xu, Recent Progress in Understanding Solid Electrolyte Interphase on Lithium Metal Anodes, *Adv. Energy Mater.*, 2021, **11**, 2003092.

16 H. R. Cheng, Q. J. Sun, L. L. Li, Y. G. Zou, Y. Q. Wang, T. Cai, F. Zhao, G. Liu, Z. Ma, W. Wahyudi, Q. Li and J. Ming, Emerging Era of Electrolyte Solvation Structure and Interfacial Model in Batteries, *ACS Energy Lett.*, 2022, **7**, 490–513.

17 J. R. Wu, Z. Y. Gao, Y. Tian, Y. Zhao, Y. L. Lin, K. Wang, H. Guo, Y. F. Pan, X. S. Wang, F. Y. Kang, N. Tavajohi, X. L. Fan and B. H. Li, Unique Tridentate Coordination Tailored Solvation Sheath Toward Highly Stable Lithium Metal Batteries, *Adv. Mater.*, 2023, **35**, 2303347.

18 X. M. Lu, Y. N. Cao, Y. Sun, H. C. Wang, W. W. Sun, Y. Xu, Y. Wu, C. Yang and Y. Wang, sp-Carbon-Conjugated Organic Polymer as Multifunctional Interfacial Layers for Ultra-Long Dendrite-Free Lithium Metal Batteries, *Angew. Chem., Int. Ed.*, 2024, **63**, e202320259.

19 W. L. Zhang, Y. Lu, L. Wan, P. Zhou, Y. C. Xia, S. S. Yan, X. X. Chen, H. Y. Zhou, H. Dong and K. Liu, Engineering a Passivating Electric Double Layer for High Performance Lithium Metal Batteries, *Nat. Commun.*, 2022, **13**, 2029.

20 J. Zhao, M. Hong, Z. J. Ju, X. Z. Yan, Y. Z. Gai and Z. Liang, Durable Lithium Metal Anodes Enabled by Interfacial Layers Based on Mechanically Interlocked Networks Capable of Energy Dissipation, *Angew. Chem., Int. Ed.*, 2022, **61**, e202214386.

21 P. Hu, W. Chen, Y. Wang, T. Chen, X. H. Qian, W. Q. Li, J. Y. Chen and J. J. Fu, Fatigue-Free and Skin-like Supramolecular Ion-Conductive Elastomeric Interphases for Stable Lithium Metal Batteries, *ACS Nano*, 2023, **17**, 16239–16251.

22 L. S. Fan, B. Sun, K. Yan, P. Xiong, X. Guo, Z. K. Guo, N. Q. Zhang, Y. J. Feng, K. N. Sun and G. X. Wang, A Dual-Protective Artificial Interface for Stable Lithium Metal Anodes, *Adv. Energy Mater.*, 2021, **11**, 2102242.

23 J. H. Li, Y. F. Cai, H. M. Wu, Z. Yu, X. Z. Yan, Q. H. Zhang, T. D. Z. Gao, K. Liu, X. D. Jia and Z. N. Bao, Polymers in Lithium-Ion and Lithium Metal Batteries, *Adv. Energy Mater.*, 2021, **11**, 2003239.

24 B. Hu, J. Xu, Z. J. Fan, C. Xu, S. C. Han, J. X. Zhang, L. B. Ma, B. Ding, Z. C. Zhuang, Q. Kang and X. G. Zhang, Covalent Organic Framework Based Lithium-Sulfur Batteries: Materials, Interfaces, and Solid-State Electrolytes, *Adv. Energy Mater.*, 2023, **13**, 2203540.

25 J. Xue, Z. Sun, B. Sun, C. Zhao, Y. Yang, F. Huo, A. Cabot, H. K. Liu and S. Dou, Covalent Organic Framework-Based Materials for Advanced Lithium Metal Batteries, *ACS Nano*, 2024, **18**, 17439–17468.

26 Y. N. Cao, Q. Xu, Y. Sun, J. X. Shi, Y. Xu, Y. F. Tang, X. D. Chen, S. Yang, Z. Jiang, H. D. Um, X. P. Li and Y. Wang, Steering Lithium and Potassium Storage Mechanism in Covalent Organic Frameworks by Incorporating Transition Metal Single Atoms, *Proc. Natl. Acad. Sci. U. S. A.*, 2024, **121**, e2315407121.

27 Y. Zheng, S. Xia, F. Dong, H. Sun, Y. Pang, J. Yang, Y. Huang and S. Zheng, High Performance Li Metal Anode Enabled by Robust Covalent Triazine Framework-Based Protective Layer, *Adv. Funct. Mater.*, 2021, **31**, 2006159.

28 L. Yue, X. Wang, L. Chen, D. Shen, Z. Shao, H. Wu, S. Xiao, W. Liang, Y. Yu and Y. Li, In situ interface engineering of highly nitrogen-rich triazine-based covalent organic frameworks for an ultra-stable, dendrite-free lithium-metal anode, *Energy Environ. Sci.*, 2024, **17**, 1117–1131.

29 X.-M. Lu, H. Wang, Y. Sun, Y. Xu, W. Sun, Y. Wu, Y. Zhang, C. Yang and Y. Wang, Covalent Triazine Based Frameworks with Donor-Donor-π-Acceptor Structures for Dendrite-Free Lithium Metal Batteries, *Angew. Chem., Int. Ed.*, 2024, **63**, e202409436.

30 Z. Lu, Q. Liang, B. Wang, Y. Tao, Y. Zhao, W. Lv, D. Liu, C. Zhang, Z. Weng, J. Liang, H. Li and Q.-H. Yang, Graphitic Carbon Nitride Induced Micro-Electric Field for Dendrite-Free Lithium Metal Anodes, *Adv. Energy Mater.*, 2019, **9**, 1803186.

31 K. Y. Geng, T. He, R. Y. Liu, S. Dalapati, K. T. Tan, Z. P. Li, S. S. Tao, Y. F. Gong, Q. H. Jiang and D. L. Jiang, Covalent Organic Frameworks: Design, Synthesis, and Functions, *Chem. Rev.*, 2020, **120**, 8814–8933.

32 C. H. Zhang, J. Y. Xie, C. T. Zhao, Y. X. Yang, Q. An, Z. Y. Mei, Q. J. Xu, Y. Q. Ding, G. F. Zhao and H. Guo, Regulating the Lithium Ions' Local Coordination Environment through Designing a COF with Single Atomic Co Site to Achieve Dendrite-Free Lithium-Metal Batteries, *Adv. Mater.*, 2023, **35**, 2304511.

33 Y. N. Cao, H. Y. Fang, C. F. Guo, W. W. Sun, Y. Xu, Y. Wu and Y. Wang, Alkynyl Boosted High-Performance Lithium Storage and Mechanism in Covalent Phenanthroline Framework, *Angew. Chem., Int. Ed.*, 2023, **62**, e202302143.

34 L. He, T. Naren, L. Zhang, F. Kang, J. Yang, Z. Chen, A. Yu, D.-S. Li, L. Chen and Q. Zhang, Interweaving Covalent Organic Polymer Chains Into Two-Dimensional Networks: Synthesis, Single Crystal Structure, and Application for Stabilizing Lithium Metal Anode, *Angew. Chem., Int. Ed.*, 2025, **64**, e202506036.

35 S. Xu, T. Naren, Y. Zhao, Q. Gu, T. Wai Lau, C.-S. Lee, F.-R. Chen, J. Yin, L. Chen and Q. Zhang, Soluble Covalent Organic Frameworks as Efficient Lithiophilic Modulator for High-Performance Lithium Metal Batteries, *Angew. Chem., Int. Ed.*, 2025, **64**, e202422040.

36 S. Che and L. Fang, Porous Ladder Polymer Networks, *Chem*, 2020, **6**, 2558–2590.

37 M. C. Wang, S. Fu, P. Petkov, Y. B. Fu, Z. T. Zhang, Y. N. Liu, J. Ma, G. B. Chen, S. M. Gali, L. Gao, Y. Lu, S. Paasch, H. X. Zhong, H. P. Steinrück, E. Cánovas, E. Brunner, D. Beljonne, M. Bonn, H. I. Wang, R. H. Dong and X. L. Feng, Exceptionally High Charge Mobility in Phthalocyanine-Based Poly(benzimidazobenzophenanthroline)-Ladder-Type Two-

Dimensional Conjugated Polymers, *Nat. Mater.*, 2023, **22**, 880–887.

38 X. L. Liu, H. Yang, H. Harb, R. Samajdar, T. J. Woods, O. Lin, Q. Chen, A. I. B. Romo, J. Rodríguez-López, R. S. Assary, J. S. Moore and C. M. Schroeder, Shape-Persistent Ladder Molecules Exhibit Nanogap-Independent Conductance in Single-Molecule Junctions, *Nat. Chem.*, 2024, **16**, 1772–1780.

39 S.-J. Kim, J. Mahmood, C. Kim, G.-F. Han, S.-W. Kim, S.-M. Jung, G. Zhu, J. J. De Yoreo, G. Kim and J.-B. Baek, Defect-Free Encapsulation of Fe0 in 2D Fused Organic Networks as a Durable Oxygen Reduction Electrocatalyst, *J. Am. Chem. Soc.*, 2018, **140**, 1737–1742.

40 V. A. Kuehl, P. H. H. Duong, D. Sadrieva, S. A. Amin, Y. She, K. D. Li-Oakey, J. L. Yarger, B. A. Parkinson and J. O. Hoberg, Synthesis, Postsynthetic Modifications, and Applications of the First Quinoxaline-Based Covalent Organic Framework, *ACS Appl. Mater. Interfaces*, 2021, **13**, 37494–37499.

41 J. He, M. J. Shi, H. X. Wang, H. Liu, J. Yang, C. Yan, J. X. Zhao, J. L. Yang and X. L. Wu, Ladder-Type Redox-Active Polymer Achieves Ultra-Stable and Fast Proton Storage in Aqueous Proton Batteries, *Angew. Chem., Int. Ed.*, 2024, **63**, e202410568.

42 X. L. Chen, M. Xie, Z. L. Zheng, X. Luo, H. C. Jin, Y. F. Chen, G. Z. Yang, D. S. Bin and D. Li, Multiple Accessible Redox-Active Sites in a Robust Covalent Organic Framework for High-Performance Potassium Storage, *J. Am. Chem. Soc.*, 2023, **145**, 5105–5113.

43 D. Wei, F. S. Ma, R. Wang, S. Y. Dou, P. Cui, H. Huang, J. Ji, E. D. Jia, X. J. Jia, S. Sajid, A. M. Eiseman, L. H. Chu, Y. F. Li, B. Jiang, J. Qiao, Y. B. Yuan and M. C. Li, Ion-Migration Inhibition by the Cation–π Interaction in Perovskite Materials for Efficient and Stable Perovskite Solar Cells, *Adv. Mater.*, 2018, **30**, 1707583.

44 X.-X. Luo, W.-H. Li, H.-J. Liang, H.-X. Zhang, K.-D. Du, X.-T. Wang, X.-F. Liu, J.-P. Zhang and X.-L. Wu, Covalent Organic Framework with Highly Accessible Carbonyls and π-Cation Effect for Advanced Potassium-Ion Batteries, *Angew. Chem., Int. Ed.*, 2022, **61**, e202117661.

45 B. Yang, X. Deng, K. Cui, X. Yang, C. Zhang, Y. Niu, Y. Liu and N. Fu, Highly crystalline covalent organic framework nanosheets with multiple redox-active sites and the cation–π effect for safe potassium-ion batteries, *J. Mater. Chem. A*, 2025, **13**, 32197–32206.

46 S. Kandambeth, J. T. Jia, H. Wu, V. S. Kale, P. T. Parvatkar, J. Czaban-Józwiak, S. Zhou, X. M. Xu, Z. O. Ameur, E. Abou-Hamad, A. H. Emwas, O. Shekhah, H. N. Alshareef and M. Eddaoudi, Covalent Organic Frameworks as Negative Electrodes for High-Performance Asymmetric Supercapacitors, *Adv. Energy Mater.*, 2020, **10**, 2001673.

47 A. Ozden, J. Li, S. Kandambeth, X. Y. Li, S. J. Liu, O. Shekhah, P. F. Ou, Y. Z. Finfrock, Y. K. Wang, T. Alkayyali, F. P. G. de Arquer, V. S. Kale, P. M. Bhatt, A. H. Ip, M. Eddaoudi, E. H. Sargent and D. Sinton, Energy- and carbon-efficient CO_2/CO electrolysis to multicarbon products via asymmetric ion migration-adsorption, *Nat. Energy*, 2023, **8**, 179–190.

48 P. T. Parvatkar, S. Kandambeth, A. C. Shaikh, I. Nadinov, J. Yin, V. S. Kale, G. Healing, A. H. Emwas, O. Shekhah, H. N. Alshareef, O. F. Mohammed and M. Eddaoudi, A Tailored COF for Visible-Light Photosynthesis of 2,3-Dihydrobenzofurans, *J. Am. Chem. Soc.*, 2023, **145**, 5074–5082.

49 Z. N. Tian, V. S. Kale, Z. X. Shi, J. Yin, S. Kandambeth, Y. Z. Wang, A. H. Emwas, Y. J. Lei, X. R. Guo, J. Ming, W. X. Wang, N. Alsadun, O. Shekhah, M. Eddaoudi and H. N. Alshareef, Optimized Charge Storage in Aza-Based Covalent Organic Frameworks by Tuning Electrolyte Proton Activity, *ACS Nano*, 2023, **17**, 13961–13973.

50 Y. L. Lin, H. L. Cui, C. Liu, R. Li, S. P. Wang, G. M. Qu, Z. Q. Wei, Y. H. Yang, Y. X. Wang, Z. J. Tang, H. F. Li, H. Y. Zhang, C. Y. Zhi and H. M. Lv, A Covalent Organic Framework as a Long-life and High-Rate Anode Suitable for Both Aqueous Acidic and Alkaline Batteries, *Angew. Chem., Int. Ed.*, 2023, **62**, e202218745.

51 W. X. Wang, V. S. Kale, Z. Cao, S. Kandambeth, W. L. Zhang, J. Ming, P. T. Parvatkar, E. Abou-Hamad, O. Shekhah, L. Cavallo, M. Eddaoudi and H. N. Alshareef, Phenanthroline Covalent Organic Framework Electrodes for High-Performance Zinc-Ion Supercapattery, *ACS Energy Lett.*, 2020, **5**, 2256–2264.

52 Z. L. Ye, S. J. Xie, Z. Y. Cao, L. P. Wang, D. X. Xu, H. Zhang, J. Matz, P. Dong, H. Y. Fang, J. F. Shen and M. X. Ye, High-Rate Aqueous Zinc-Organic Battery Achieved by Lowering HOMO/LUMO of Organic Cathode, *Energy Storage Mater.*, 2021, **37**, 378–386.

53 X. Y. Ni, J. Liu, H. Q. Ji, L. B. Chen, T. Qian and C. L. Yan, Ordered Lithium Ion Channels of Covalent Organic Frameworks with Lithiophilic Groups Enable Uniform and Efficient Li Plating/Stripping, *J. Energy Chem.*, 2021, **61**, 135–140.

54 Y. R. Zhang, W. B. Wang, M. L. Hou, Y. T. Zhang, Y. Y. Dou, Z. H. Yang, X. Y. Xu, H. N. Liu and S. L. Qiao, Self-Exfoliated Covalent Organic Framework Nano-Mesh Enabled Regular Distribution for Stable Lithium Metal, *Energy Storage Mater*, 2022, **47**, 376–385.

55 K. S. Oh, S. Park, J. S. Kim, Y. Yao, J. H. Kim, J. Guo, D. H. Seo and S. Y. Lee, Electrostatic Covalent Organic Frameworks as On-Demand Molecular Traps for High-Energy Li Metal Battery Electrodes, *ACS Energy Lett.*, 2023, **8**, 2463–2474.

56 D. D. Chen, S. Huang, L. Zhong, S. J. Wang, M. Xiao, D. M. Han and Y. Z. Meng, In Situ Preparation of Thin and Rigid COF Film on Li Anode as Artificial Solid Electrolyte Interphase Layer Resisting Li Dendrite Puncture, *Adv. Funct. Mater. Materials*, 2020, **30**, 1907717.

57 W. B. Wang, Z. H. Yang, Y. T. Zhang, A. P. Wang, Y. R. Zhang, L. L. Chen, Q. Li and S. L. Qiao, Highly Stable Lithium Metal Anode Enabled by Lithiophilic and Spatial-Confined Spherical-Covalent Organic Framework, *Energy Storage Mater.*, 2022, **46**, 374–383.

58 Y. T. Zhang, Z. H. Yang, Y. Y. Dou, W. B. Wang, Y. R. Zhang, A. P. Wang, X. J. Zhang, X. M. Guo and S. L. Qiao, Hollow Spherical Organic Polymer Artificial Layer Enabled Stable Li Metal Anode, *Chem.–Eng. J.*, 2022, **442**, 136155.

59 G. H. Li, Y. Yang, J. C. Cai, T. Wen, L. C. Zhuang, X. Y. Huang, Y. P. Cai and X. J. Hong, Lithiophilic Aromatic Sites and Porosity of COFs for a Stable Lithium Metal Anode, *ACS Appl. Energy Mater.*, 2022, **5**, 13554–13561.

60 X. Y. Wu, S. Q. Zhang, X. Y. Xu, F. X. Wen, H. W. Wang, H. Z. Chen, X. L. Fan and N. Huang, Lithiophilic Covalent Organic Framework as Anode Coating for High-Performance Lithium Metal Batteries, *Angew. Chem., Int. Ed.*, 2024, **63**, e202319355.

61 Y. W. Song, P. Shi, B. Q. Li, X. Chen, C. X. Zhao, W. J. Chen, X. Q. Zhang, X. Chen and Q. Zhang, Covalent Organic Frameworks Construct Precise Lithiophilic Sites for Uniform Lithium Deposition, *Matter*, 2021, **4**, 253–264.

62 X. R. Li, Y. Tian, L. Shen, Z. B. Qu, T. Q. Ma, F. Sun, X. Y. Liu, C. Zhang, J. Q. Shen, X. Y. Li, L. N. Gao, S. X. Xiao, T. F. Liu, Y. Liu and Y. F. Lu, Electrolyte Interphase Built from Anionic Covalent Organic Frameworks for Lithium Dendrite Suppression, *Adv. Funct. Mater.*, 2021, **31**, 2009718.

63 C. Li, D. D. Wang, G. Ho, Z. Y. Zhang, J. Huang, K. T. Bang, C. Y. Lau, S. Y. Leu, Y. M. Wang and Y. Kim, Anthraquinone-Based Silicate Covalent Organic Frameworks as Solid Electrolyte Interphase for High-Performance Lithium-Metal Batteries, *J. Am. Chem. Soc.*, 2023, **145**, 24603–24614.

64 Z. H. Li, W. Y. Ji, T. X. Wang, Y. R. Zhang, Z. Li, X. S. Ding, B. H. Han and W. Feng, Guiding Uniformly Distributed Li-Ion Flux by Lithiophilic Covalent Organic Framework Interlayers for High-Performance Lithium Metal Anodes, *ACS Appl. Mater. Interfaces*, 2021, **13**, 22586–22596.

65 Y. X. Zheng, S. X. Xia, F. Dong, H. Sun, Y. P. Pang, J. H. Yang, Y. Z. Huang and S. Y. Zheng, High Performance Li Metal Anode Enabled by Robust Covalent Triazine Framework-Based Protective Layer, *Adv. Funct. Mater.*, 2021, **31**, 2006159.

66 X. D. Li, Y. T. Zhang, Y. Y. Dou, Z. Y. Zhao, X. Y. Fan and H. C. Jiang, Nanoporous Triazine-Framework-Assembled Electrolyte Interphase Layer as a Lithiophilic Gridding for Uniform Lithium Deposition and Dendrite Inhibition, *ACS Applied Nano Mater*, 2024, **7**, 2825–2835.

67 S. Q. Zhang, R. H. Li, N. Hu, T. Deng, S. T. Weng, Z. C. Wu, D. Lu, H. K. Zhang, J. B. Zhang, X. F. Wang, L. X. Chen, L. W. Fan and X. L. Fan, Tackling Realistic Li^+ Flux for High-Energy Lithium Metal Batteries, *Nat. Commun.*, 2022, **13**, 5431.

68 J. Y. Zheng, L. Y. Duan, H. Ma, Q. An, Q. Liu, Y. J. Sun, G. F. Zhao, H. L. Tang, Y. Li, S. M. Wang, Q. J. Xu, L. L. Wang and H. Guo, Leveraging Polymer Architecture Design with Acylamino Functionalization for Electrolytes to Enable Highly Durable Lithium Metal Batteries, *Energy Environ. Sci.*, 2024, **17**, 6739–6754.

69 M. D. Tikekar, L. A. Archer and D. L. Koch, Stabilizing Electrodeposition in Elastic Solid Electrolytes Containing Immobilized Anions, *Sci. Adv.*, 2016, **2**, e1600320.

70 A. X. Wang, Y. X. Nie, Y. M. Zhao, D. H. Xu, L. X. Zhang, Z. F. Zhao, L. B. Ren, S. B. Zhou, X. J. Liu and J. Y. Luo, Functional Copolymer Derived Self-Adapting LiF-Rich Interphase Toward Deep Cycling Lithium Metal Batteries, *Adv. Funct. Mater.*, 2024, **34**, 2401462.

71 M. W. Leng and L. Fang, Semiconducting ladder-type covalent organic frameworks, *Chem*, 2022, **8**, 2904–2906.

72 Y. F. Wang, Z. L. Qiao, K. X. Liu, L. Yu, Y. Y. Lv, L. Y. Shi, Y. Zhao, D. P. Cao, Z. Y. Wang, S. T. Wang and S. Yuan, High-Rate Organic Cathode Constructed by Iron-Hexaazatrinaphthalene Tricarboxylic Acid Coordination Polymer for Li-Ion Batteries, *Adv. Sci.*, 2022, **9**, 2205069.

73 H. Li, D. L. Chao, B. Chen, X. Chen, C. Chuah, Y. H. Tang, Y. Jiao, M. Jaroniec and S. Z. Qiao, Revealing Principles for Design of Lean-Electrolyte Lithium Metal Anode via In Situ Spectroscopy, *J. Am. Chem. Soc.*, 2020, **142**, 2012–2022.

74 S. Zheng, S. Bi, Y. B. Fu, Y. Wu, M. H. Liu, Q. Xu and G. F. Zeng, 3D Crown Ether Covalent Organic Framework as Interphase Layer toward High-Performance Lithium Metal Batteries, *Adv. Mater.*, 2024, **36**, 2313076.

75 Y. Y. Liu, Y. K. Tzeng, D. C. Lin, A. Pei, H. Y. Lu, N. A. Melosh, Z. X. Shen, S. Chu and Y. Cui, An Ultrastrong Double-Layer Nanodiamond Interface for Stable Lithium Metal Anodes, *Joule*, 2018, **2**, 1595–1609.

76 S. M. Li, J. L. Huang, Y. Cui, S. H. Liu, Z. R. Chen, W. Huang, C. F. Li, R. L. Liu, R. W. Fu and D. C. Wu, A Robust All-Organic Protective Layer towards Ultrahigh-Rate and Large-Capacity Li Metal Anodes, *Nat. Nanotechnol.*, 2022, **17**, 613–621.